International Journal of Plasticity 129 (2020) 102696

Contents lists available at ScienceDirect

International Journal of Plasticity

journal homepage: http://www.elsevier.com/locate/ijplas

Strain rate sensitivity of the ultrastrong gradient nanocrystalline 316L stainless steel and its rate-dependent modeling at nanoscale

Fei Yin [a,b,c,1], Shan Hu [c,1], Rong Xu [c], Xinghui Han [a,b], Dongsheng Qian [a,b], Wenting Wei [a,b], Lin Hua [a,b,*], Kejie Zhao [c,**]

[a] Hubei Key Laboratory of Advanced Technology for Automotive Components, Wuhan University of Technology, Wuhan, 430070, China
[b] Hubei Collaborative Innovation Center for Automotive Components Technology, Wuhan University of Technology, Wuhan, 430070, China
[c] School of Mechanical Engineering, Purdue University, West Lafayette, IN, 47907, USA

ARTICLE INFO

Keywords:
Nanocrystalline steel
Strain rate sensitivity
Grain boundary activities
Mechanical strengthening
Constitutive modeling

ABSTRACT

We fabricate ultrastrong gradient nanocrystalline (NC) 316L stainless steel with an extremely fined grain size of 5 nm using the Ultrasonic Strain Engineering Technology (USET) at ambient temperature. We evaluate the strain rate sensitivity (SRS), an indicator of the rate controlling mechanism in the plastic deformation of metals and alloys, for the ultrastrong gradient NC 316L stainless steel by strain rate jump nanoindentation and micropillar compression test. The significant decrease of the SRS for the NC 316L stainless steel with a grain size of 5 nm is attributed to the phase transformation from the austenite face center cubic (FCC) to the martensite body center cubic (BCC) structures during the grain refinement process. In addition, the grain boundary activities in NC 316L stainless steel is largely suppressed by the embodied nanosized intermetallic phases and metal precipitates. We propose an in-situ grain structure stability mechanism to achieve such extremely fined NC stainless steel via USET at ambient temperature. We further adopt and validate a rate-dependent constitutive model for the NC 316L stainless steel. The work provides an efficient way to produce ultrastrong gradient NC 316L stainless steel that can be widely used in the light-weighting and mechanical strengthening of aerospace and transportation engineering.

1. Introduction

Nanocrystalline (NC) metals and alloys fabricated using the severe plastic deformation (SPD) are emerging materials of extraordinary physical and chemical properties (Liu et al., 2015; Meredith and Khan, 2012; Ovid'Ko and Sheinerman, 2017; Ovid'Ko et al., 2018; Yuan et al., 2019). The mechanical behavior of the NC metals and alloys has raised tremendous interest in mechanical engineering and materials science (Dao et al., 2007; Khan et al., 2006; Liu et al., 2015; Lu et al., 2019; Padilla and Boyce, 2010). It is acknowledged that the mechanical response of the NC materials is rate-dependent (Farrokh and Khan, 2009; Khan and Meredith, 2010). A reliable rate-dependent material model is important for the theoretical understanding of the gradient NC steel in multiscale

* Corresponding author. Hubei Key Laboratory of Advanced Technology for Automotive Components, Wuhan University of Technology, Wuhan, 430070, China.
** Corresponding author.
E-mail addresses: hualin@whut.edu.cn (L. Hua), kjzhao@purdue.edu (K. Zhao).
[1] Equal contribution to this work.

https://doi.org/10.1016/j.ijplas.2020.102696
Received 15 November 2019; Received in revised form 21 January 2020; Accepted 31 January 2020
Available online 6 February 2020

plasticity (Li and Soh, 2012; Lu et al., 2019; McDowell, 2010). The deformation mechanism of the NC metals and alloys at nanoscale, especially at the length scale of less than 20 nm, is complex due to the competing dislocation-mediated and grain boundary-dominated activities. The strain-rate sensitivity (SRS) can provide valuable insight on the deformation mechanism of the metallic alloys of ultrafine grained (UFG) and/or NC grained structure at multiple length scales (Mohebbi and Akbarzadeh, 2017; Zhang et al., 2013; Zhao et al., 2018) and further fingerprints the rate controlling mechanism during the thermally activated process of the UFG/NC materials (Maier-Kiener and Durst, 2017). SRS is defined as the change of the stress σ divided by the change of the strain rate $\dot{\varepsilon}$ at constant temperature (Maier et al., 2011):

$$m = \frac{d(ln\sigma)}{d(ln\dot{\varepsilon})}, \tag{1}$$

where m represents the SRS exponent.

The experimental and theoretical studies of the SRS of metals and alloys of the UFG and NC structures have been a subject of extensive research (Huang et al., 2010; Mohebbi and Akbarzadeh, 2017; Zhang et al., 2016). The value of the SRS exponent m can be determined by strain-rate jump experiments during a single test or experiments with several uniaxial compression/tensile tests at different strain rates (Khan and Liu, 2012; Maier et al., 2011; Mohebbi and Akbarzadeh, 2017). For example, Kabirian et al. studied the thermo-mechanical response of an AA 5182-O sheet using the uniaxial tension and compression tests under both quasi-static and dynamic loading. They captured the transition of the SRS from a negative to a positive value in the AA 5182-O sheet when dynamically loaded under different temperatures, which is critical for the accurate constitutive modeling for the 5xxx series aluminum alloys (Kabirian et al., 2014). Khan et al. fabricated high-quality bulk ultra-fine grained and NC pure aluminum samples at room temperature. They found that the SRS of the samples increased as the grain size was reduced to the nanometer scale, and furthermore, the flow stress was significantly influenced by the grain size (Khan et al., 2008). Schwaiger et al. revealed a strong dependence of SRS on the grain size of the NC-Ni by systematically comparing the nanoindentation and tensile experiments results. They stated that, while the microcrystalline and ultra-fine crystalline pure Ni exhibited a strain rate independent plastic flow (flow rate in the range of 3×10^{-4}–3×10^{-1} s^{-1}), NC pure Ni with a grain size of ~40 nm showed marked rate sensitivity of plastic flow (Schwaiger et al., 2003). Huang et al. observed a significantly enhanced SRS of NC copper and attributed this abnormal behavior to the competition of the grain boundary sliding and dislocation activities of the NC copper (Huang et al., 2010). The enhanced SRS implied that the increased dislocation density largely accommodated the thermally activated deformation and resulted in a lower activation volume of the NC/UFG metals and alloys (Miyamoto et al., 2006; Xu et al., 2015).

316L austenite stainless steel has been widely used in the automotive, nuclear, aerospace, and biomedical engineering (Li et al., 2019; Rakita et al., 2013; Yin et al., 2016, 2017, 2018c). It presents the major advantages of excellent corrosion resistance, low cost, and great formability. The mechanical strength of 316L austenite stainless steel can be significantly improved by grain refinement. Chen et al. fabricated 316L NC stainless steel with the average grain size of 40 nm and confirmed that the yield strength of the nanograined materials can reach 1.45 GPa (Chen et al., 2005). Yin el al. produced NC 316L stainless steel with the average grain size of 25 nm. The yield strength of the devised NC 316L stainless steel can reach up to 1.9 GPa, which is nearly 8 times higher than that of its coarse-grained counterpart (Yin et al., 2018a). A unique feature is that the gradient architecture is free of a sharp interface between the NC surface layer and the coarse-grained matrix. The material exhibits elastically homogeneous but plastically gradient behavior which provides a unique way of measuring the intrinsic tensile plasticity of nanograined metals without strain localization (Fang et al., 2011). The enhanced fatigue life of the gradient NC 316L stainless steel was reported recently (Lei et al., 2019; Ueno et al., 2011; Zhou et al., 2017). The extraordinary mechanical properties and unique characteristics make gradient NC 316L stainless steel an ideal high-performance metal that can be widely used for light-weighting and mechanical strengthening in a variety of engineering applications.

Several groups recently investigated the effect of the grain size and microstructure of the 316L stainless steel on its SRS. It is found that the coarser grain structure and more microstructural heterogeneity led to a lower value of SRS of the 316L stainless steel (Khodabakhshi et al., 2019). The finer microstructural length scale, rather than the average grain size, is the key factor to determine the tensile plasticity of the material (Li et al., 2019). The measured average grain size of these 316L stainless steels is typically at the scale of micrometers. The deformation mechanism of the 316L stainless steel at nanoscale is still unclear and systematic studies of the SRS of the gradient NC 316L stainless steel across multiple length scales have never been reported. Challenges to measure the SRS of the 316L stainless steel at different length scales include (a) fabrication of the gradient NC sample with different grain structures and consist of nanosized grains and ultrafine grains in one sample to eliminate the variations from the sample preparation, (b) fabrication of the extremely fined NC 316L stainless steel with the average grain size less than 20 nm in order to measure the SRS in the extremely fined grain structures, and (c) lack of advanced mechanical test method that can minimize the thermal drift during the low strain-rate tests to obtain the accurate SRS of the materials from nanoscale to microscale.

Herein we report a systematic investigation of the SRS of gradient NC 316L stainless steel at multiple length scales. The gradient NC 316L stainless steel with the average grain size from 5 nm to hundreds of nanometers is successfully fabricated using the USET at ambient temperature. We achieve a breakthrough in synthesizing bulk NC steel with extremely fined grain structure down to several nanometers. An in-situ grain structure stability mechanism during the USET at ambient temperature is proposed and identified using the STEM-EDS at nanoscale. Furthermore, we measure the mechanical behavior of the gradient NC steel using the nanohardness and micro-pillar compression tests at different length scales. We perform strain-rate jump nanoindentation to determine the SRS of the gradient NC steel of the grain size from 5 nm to 30 μm and we unravel the relationship between the m-value and the grain structure of the material. We adopt and validate a rate-dependent constitutive model (Jia et al., 2003) for the NC steel based on the experimental

data, which can be used for computational modeling of the gradient NC steel under various boundary conditions in future. The new findings in this paper not only provide an efficient way to produce NC 316L stainless steel for their promising applications but also offer complete understanding of the deformation and strengthening mechanism of the NC 361 stainless steel at multiple length scales.

2. Experimental procedures

2.1. Materials and fabrication method

Fig. 1 (a) shows the characterization of the as-received (AR) 316 L stainless steel by scanning electron microscopy (SEM). Its chemical composition is measured using the EDS analysis and the inset in Fig. 1 (a) shows the spectrum of the EDS mapping. The gradient NC structure is fabricated using an optimized SPD method, e.g. ultrasonic strain engineering technology, which has been described in our previously published literature (Yin et al., 2014, 2015a, 2015b, 2017, 2018b). Hereby, high-strength chromium steel shots with the diameter of 3 mm are used in this study. They are placed on a vibrating surface driven by a high-frequency ultrasonic signal of 20 kHz. These steel shots are accelerated by the vibrating surface and impact the target surface repeatedly, resulting in severe plastic deformation of the target surface. Fig. 1 (b) illustrates the statistical analysis of the grain size distribution of the AR 316L stainless steel. The average grain size is measured to be 28 μm.

2.2. Material characterizations

SEM imaging of the samples is conducted using the FEI QUANTA 3D FEG SEM/FIB at the voltage of 5 kV with a beam spot size of 6. The sample is polished and etched according to the protocol described in our previous work (Yin et al., 2018a, 2018c). For a better image quality, all the samples are coated with a thin layer (several nanometers) of platinum using the CRESSINGTON sputter coater 208 HR. FIB channeling contrast imaging is used to characterize the gradient NC structure fabricated on the 316L stainless steel. A cross-sectional area with the width of 15 μm and length of 50 μm is firstly polished by the FIB. A current of 10 pA is supplied to minimize the damage of the polished surface. A TEM lamellar with the width of 6 μm and length of 15 μm is prepared from the topmost surface of the gradient NC steel in the SEM/FIB chamber and then lifted out using the Oxford OmniProbe 200 lift-out system. After thinning process, the TEM sample with the thickness around 100 nm is prepared and characterized by the FEI Talos 200X TEM system with the accelerate voltage of 200 kV. The chemical distribution of the NC 316L stainless steel is characterized using FEI Talos 200X TEM equipped with a FEI Super-X™ detector, which combines four symmetrically positioned Si drift detectors (SDD) around the objective lens with a high-brightness gun. Phase identification of the 316L stainless steel is performed using the Bruker D8 Focus XRD system with the Cu K-alpha source.

2.3. Mechanical tests

Nanoindenter G200 is used to measure the nanohardness of the gradient NC steel in the cross-sectional direction. The detailed experimental setup and method can be found in our previous publications (Yin et al., 2018a, 2018b, 2018c). The distance between the indents is set as 3 μm to avoid the interference of the indents in the first batch of 50 tests. In the following 50 tests, the distance between the indents is set as 5 μm. The strain rate of the test is set as 0.05 s^{-1}. The allowed thermal drift is 0.05 nm/s and the displacement into the surface is set as 2000 nm with a holding time of 2 s. Additionally, micropillars with different grain sizes are fabricated at different positions of the cross-sectional surface of the gradient NC stainless steel. The angular ion milling method is used for the fabrication of

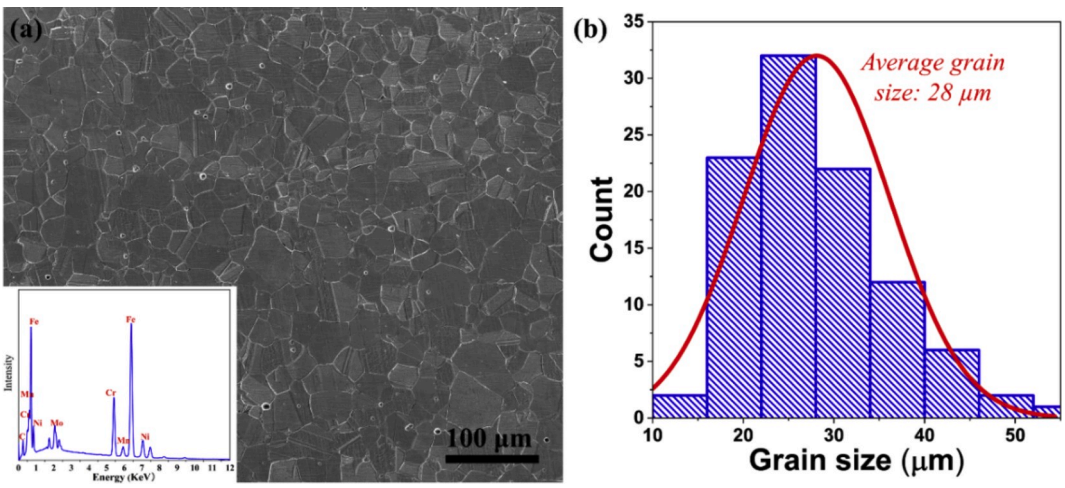

Fig. 1. (a) Material characterizations and (b) grain size distribution of the as-received coarse-grained 316L stainless steel.

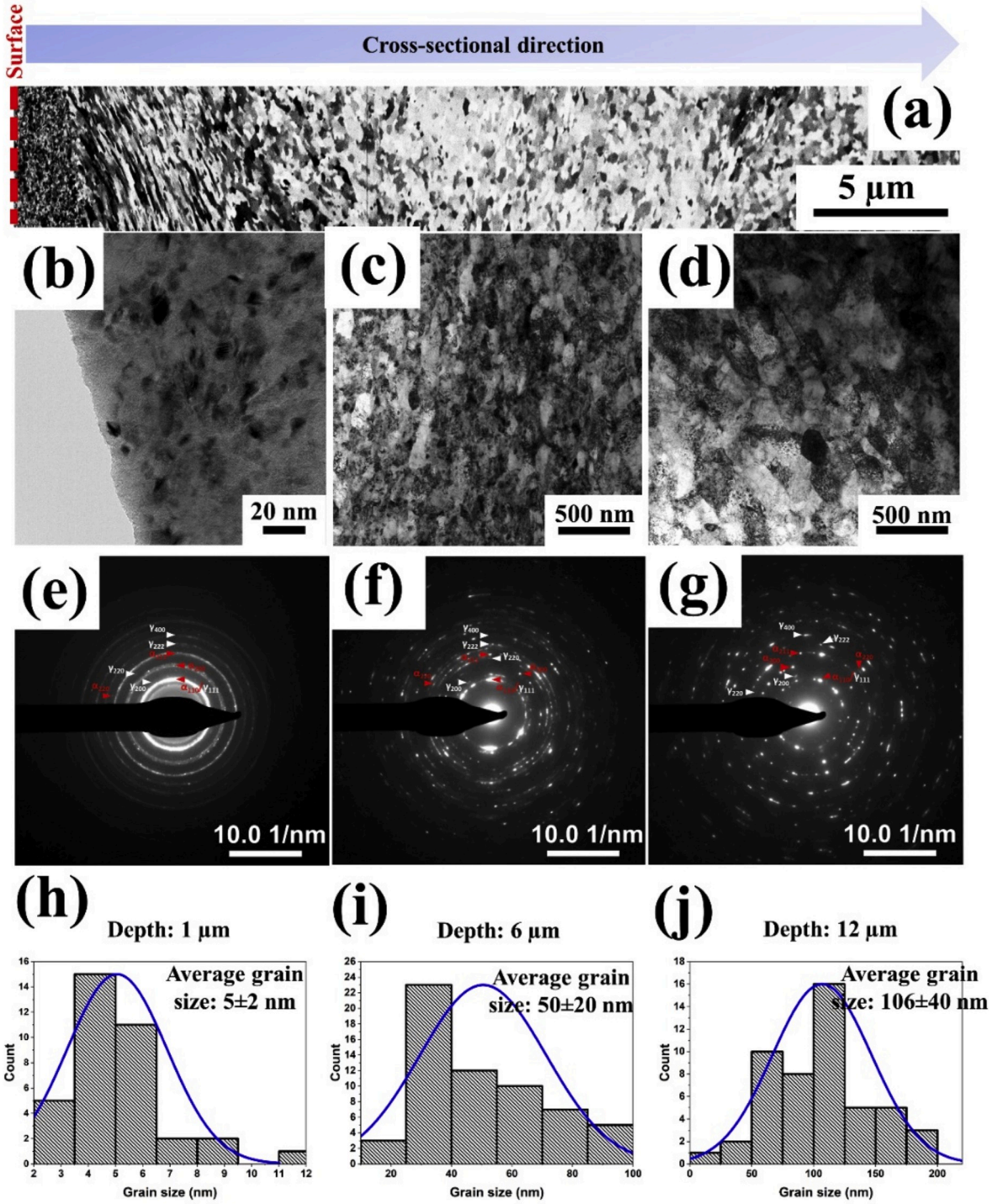

Fig. 2. (a) The gradient structure of the NC steel with a sharp transition of the average grain size observed in the FIB channeling contrast image. (b)–(d) Bright-field TEM images of the NC steel at the depth of 1 μm, 6 μm, and 12 μm, respectively, from the peening surface marked by the red dashed line in (a). (e)–(g) Indexed selected area diffraction (SAD) patterns of the microstructures shown in (b)–(d), respectively, using the same aperture size. (h)–(j) Statistical distribution of the grain size of the NC steel in the respective regimes in (b)–(d). (For interpretation of the references to colour in this figure legend, the reader is referred to the Web version of this article.)

the micropillars. A big trench of the outer and inner diameters of 40 μm and 10 μm, respectively, and depth of 6 μm is firstly ion milled using the ion milling current of 15 nA to have enough room for the displacement of the flat tip during the compression test. Then the micropillar is fabricated using an increasingly lower ion beam current in each step. Finally, the micropillar with the diameter of 3 μm and height of 6 μm is fabricated at the current of 0.1 nA to guarantee its surface quality. A flat diamond indenter tip is used for the micropillar compression test. The detailed description of the micropillar compression test can be found in our previous publications (Yin et al., 2018a, 2018c). The strain rate of the micropillar compression experiments is 0.01 s^{-1}. Advanced strain rate-jump nano-indentation is used to measure the SRS of the gradient NC stainless steel at different locations. 10 tests are conducted on the NC 316L stainless steel at the depth of 2 μm, 300 μm, and 1500 μm from the topmost peened surface with the strain rate set in the range from 0.001 s^{-1} to 0.1 s^{-1}.

3. Results

3.1. Gradient nanocrystalline steel

Fig. 2 illustrates the material characterization of the gradient NC steel fabricated by the USET. The FIB channeling contrast image provides an overview of the gradient NC structure. Fig. 2 (a) shows the FIB channeling contrast imaging of the gradient NC steel along the cross-sectional direction. The topmost surface of the sample is marked by the red dashed line. Fig. 2 (b)–(d) show the transmission electron microscopy (TEM) characterization of the NC steel at the locations of 1 μm, 6 μm, and 12 μm, away from the topmost surface. Fig. 2 (e), (f), and (g) are the indexed selected area diffraction (SAD) patterns of the NC structure in the respective areas of (b)-(d). It can be seen in the SAD patterns that with the increase of the distance from the surface, the diffraction rings gradually morph into discontinuous spots, indicating the increased grain size. The α_{110}, α_{200}, α_{220}, and α_{221} diffraction patterns are identified in Fig. 2 (e)–(g), which imply the phase transformation of the NC 316L stainless steel during the grain refinement process. Additionally, the fraction of the α phase decreases with the increase of the depth from the topmost surface of the gradient NC stainless steel. It is noted that an amorphous diffraction ring is observed in Fig. 2 (e), which is due to the FIB ion damage during the TEM sample preparation. Fig. 2 (h), (i), and (j) illustrate the statistical analysis of the grain size of the gradient NC steel at the depth of 1 μm, 6 μm, and 12 μm from the topmost surface, respectively. The average grain size and its standard deviation at the three locations are 5 ± 2 nm, 50 ± 20 nm, and 106 ± 40 nm, respectively. We point out that the average grain size of the NC steel at the topmost surface is around 5 nm, which is the finest NC steel that is ever fabricated using the SPD at ambient temperature. Considering the unstable grain structure of the NC steel due to its high grain boundary energy, it is a grand challenge to achieve such extremely fined NC steel using the SPD at ambient temperature, which always involves in an elevated temperature and high strain rate during the grain refinement process. In USET, element precipitation would take place due to the latent heat generated by the high-intense ultrasonic impacts. The element precipitation and/or grain boundary segregation will stabilize the NC grain structure by decreasing the grain boundary energy and the pinning effect, leading to the formation of the extremely fined NC structure illustrated in Fig. 2 (b). This hypothesis will be further discussed and validated using STEM/EDS analysis of the gradient NC steel at nanoscale in the following session.

Fig. 3 shows the XRD profiles of the 316L stainless steel with the coarse grained (CG) and nanograined (NG) structure. The γ_{111} austenite phase is partially transformed to α_{110} martensite phase after USET. It should be noted that all the XRD measurements are conducted at the topmost surface of the CG and NG 316L stainless steel and the volume fraction of the transformed α phase varies along the cross-sectional direction of the sample. In addition, the time dependent behavior of the phase transformation is also studied by

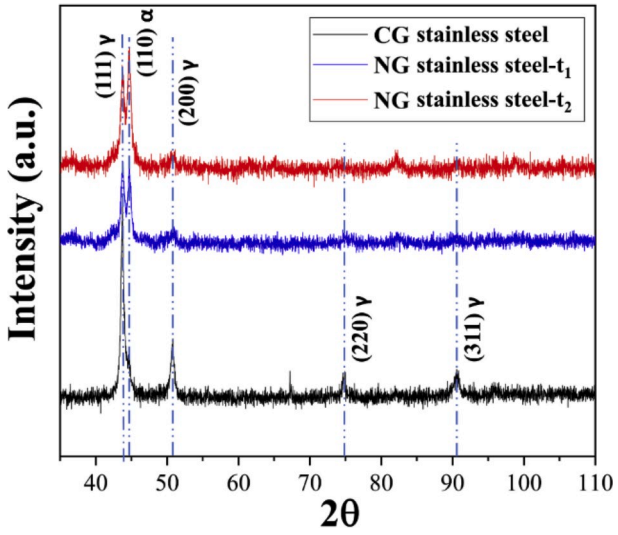

Fig. 3. XRD profiles of the as-received 316L stainless steel and the USETed 316L stainless steel surface with processing times t1 = 360s and t2 = 600s.

measuring the 316L stainless steel treated with different processing times ($t_1 = 360s$ and $t_2 = 600s$). The fraction of the (110) α phase of the NG 316L stainless steel gradually increases with the processing time as illustrated in Fig. 3.

3.2. Mechanical behaviors of the gradient NC stainless steel

Fig. 4 (a) plots the nanohardness of the gradient NC steel along the cross-sectional direction. The nanohardness gradually decreases with the distance from the topmost peening surface of the sample. The maximum nanohardness of the NC steel is around 6.2 GPa, which is located at the topmost surface. The gradient nanohardness profile agrees well with the gradient grain structure of the NC steel demonstrated in Fig. 2. Fig. 4 (b) shows the Young's modulus of the gradient NC steel along the cross-sectional direction. There is no significant change of the Young's modulus as the grain size increases. The results in figure (4) confirms the elastically homogeneous but plastically gradient nature of the NC steel fabricated by USET.

Furthermore, we conduct uniaxial compression tests of micropillars of the NC steel with different grain sizes. The micropillars are fabricated at different locations of the gradient NC steel sample. Fig. 5 (a) illustrates the EBSD mapping along the cross-sectional direction and the locations of the fabricated micropillars. Fig. 5 (b) shows the engineering stress-strain responses of the micropillars fabricated at the locations of 5 μm, 20 μm, 50 μm, 100 μm, and 1500 μm away from the topmost surface of the gradient NC 316L stainless steel. It should be noted that the results for the micropillars at the locations of 5 μm and 1500 μm have been reported by the authors in 2018 (Yin et al., 2018a). These data are used for comparison. The yield strength is not well defined in the engineering stress-strain curves in Fig. 5. We determine the relationship between the stress and the strain increment of the micropillars at the locations of (a) 5 μm, (b) 20 μm, (c) 50 μm, (d) 100 μm, (e) 500 μm, and (f) 1500 μm from the peened surface. The results are shown in Fig. 6. Hereby, the yield strength of the micropillars is defined as the stress at the turning point of the $d\varepsilon - \sigma$ curves. According to the data analysis, the yield strength of the material at the five selected locations are 1906 MPa, 1716 MPa, 1438 MPa, 1029 MPa, and 407 MPa, respectively.

We identify three strain increment modes for the deformed pillars of different grain sizes based on the $d\varepsilon - \sigma$ curves in Fig. 6 – the "smooth", "Zig-like", and "Peaks" plastic strain increment mode. To understand the mechanism underlying the three plastic strain increment modes, the deformed micropillars are characterized and illustrated in Fig. 5. Fig. 5 (c-2) - (g-2) represent the deformed micropillars at the depth of 5 μm, 20 μm, 50 μm, 100 μm, and 1500 μm from the peened surface, respectively. Fig. 5 (c-2) shows that the micropillar at the location of 5 μm and of the average grain size of 25∼30 nm is deformed uniformly and there are no visible slip bands on the deformed pillar. The grain boundaries in the nanocrystalline micropillars act as obstacles for the dislocation motion and may become dislocation sources as well. Moreover, grain boundary sliding can occur with enhanced grain boundary diffusion at nanoscale therefore the catastrophic slip events cannot take place in the nanocrystalline micropillars (Chinh et al., 2012). According to the stress-strain curves in Fig. 5 (b), strain hardening occurs during the micropillar compression of the nanocrystalline material, indicating that there is still room for dislocation accumulation at nanosized grain boundaries. The "smooth" strain increment mode is identified during the plastic deformation of the micropillar with the average grain size of 25–30 nm as shown in Fig. 6 (a). Fig. 5 (e−2) and 5 (f-2) demonstrate the deformed micropillars at the locations of 50 μm and 100 μm, respectively. Slip bands emerge on the surface of the deformed micropillars. As evident in Fig. 6 (c) and (d), the plastic strain increment mode is a combination of the "smooth" and "zig-like" characteristics. The reason is that there are not enough grain boundaries to store the moved dislocations for the micropillars with ultrafine grain structure. When the dislocations moved to the surface of the sample during compression, there will be a sudden

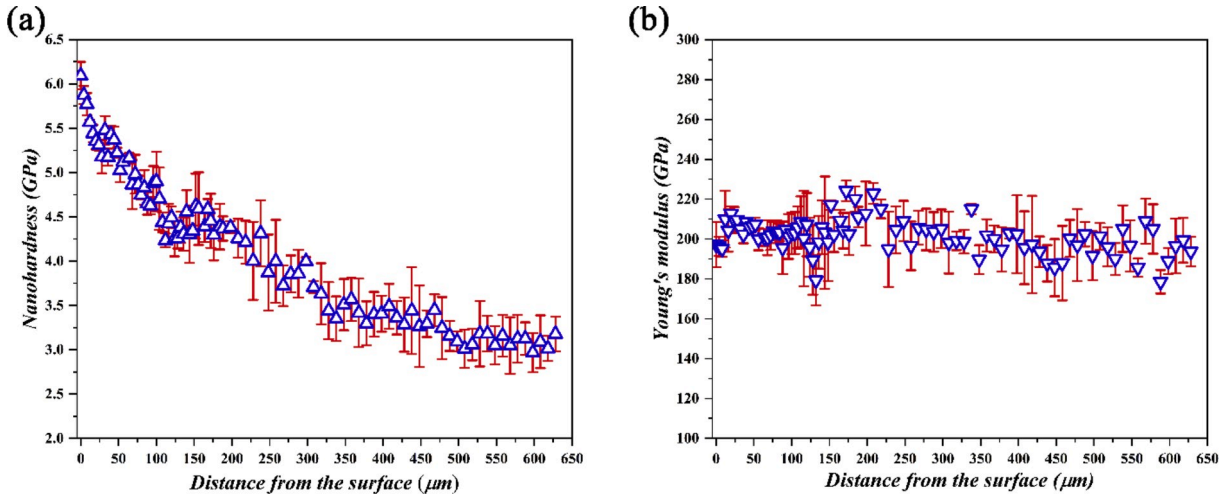

Fig. 4. (a) Nanohardness and (b) Young's modulus of the gradient NC steel along the cross-sectional direction confirming its elastically homogeneous but plastically gradient characteristics.

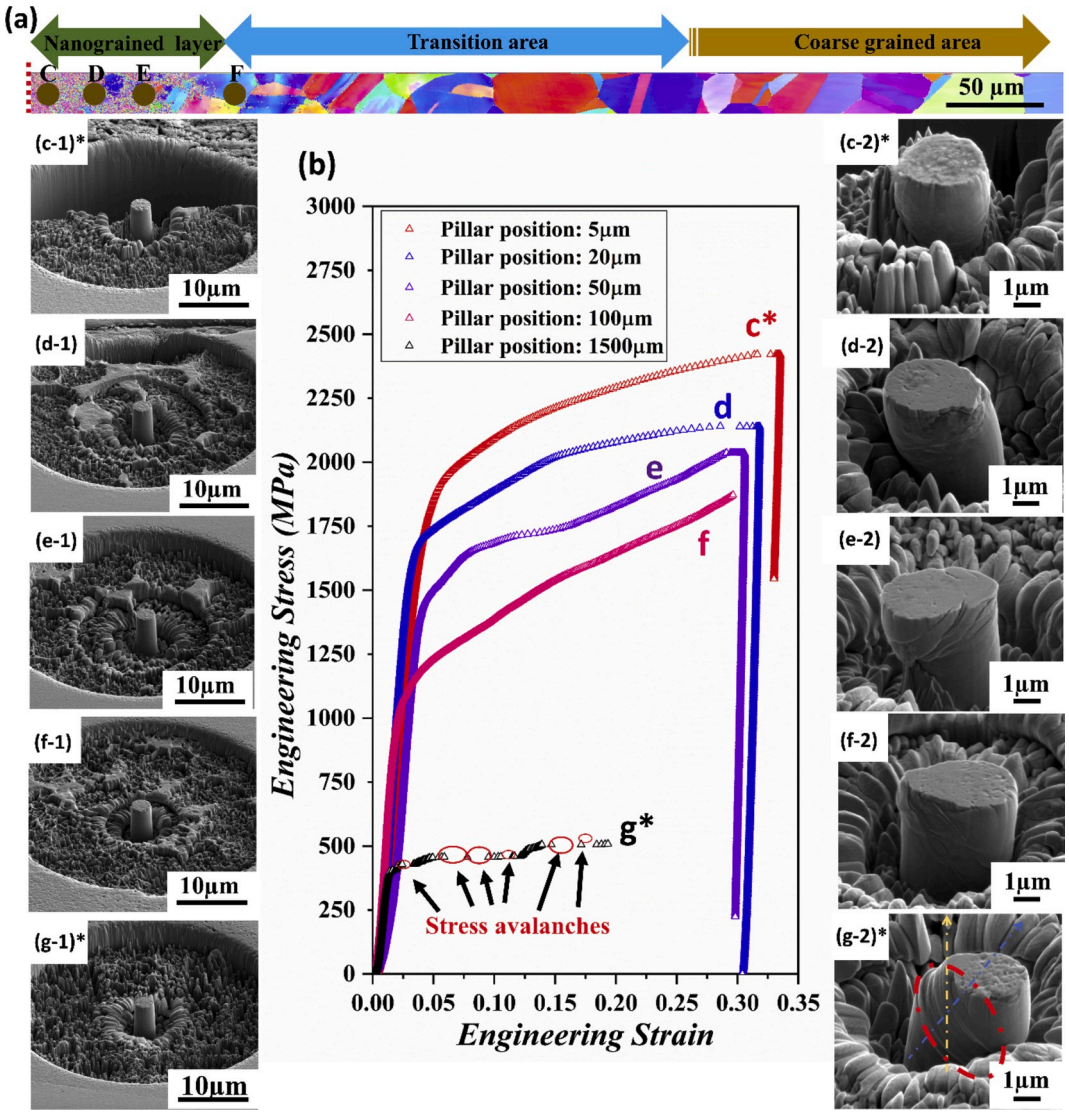

Fig. 5. Mechanical behavior of the gradient NC steel measured by the micropillar compression test at the strain rate of $0.01s^{-1}$. (a) EBSD mapping in the cross-sectional direction of the sample and the locations of the fabricated micropillars. (b) The engineering stress-strain responses of the micropillars fabricated at the depth of 5 μm, 20 μm, 50 μm, 100 μm, and 1500 μm from the topmost surface. (c)–(g) SEM images of the micropillars at the depth of 5 μm, 20 μm, 50 μm, 100 μm, and 1500 μm, respectively, from the sample surface before and after the compression test. * These results have been reported by the authors in Yin et al. (2018a).

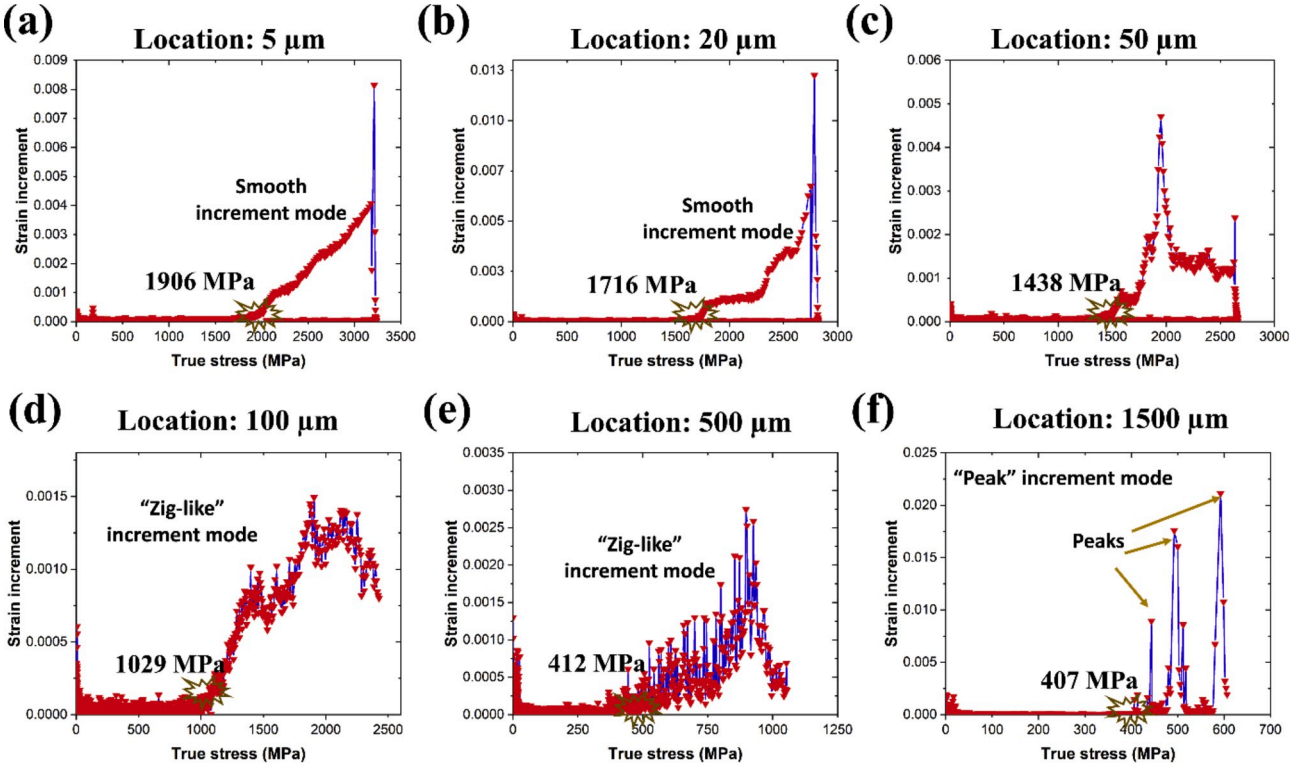

Fig. 6. The stress and strain increment curves of the micropillars fabricated at the depth of (a) 5 μm, (b) 20 μm, (c) 50 μm, (d) 100 μm, (e) 500 μm, and (f) 1500 μm from the sample surface.

pop-in of the displacement, resulting in the zig-like increment of the plastic strain. Fig. 6 (e) illustrates a typical "zig-like" plastic strain increment mode of the micropillar fabricated at the location of 500 μm. Fig. 5 (g-2) shows the microstructure of the deformed micropillar fabricated at the location of 1500 μm. As shown in Fig. 6 (f), the plastic increment mode is "peak-like". That is because there is no grain boundary in the micropillar to retain the moved dislocations. Dislocations will move to the surface of the pillar and vanish, resulting in the plastic strain increment peaks as illustrated in Fig. 6 (f). The stress avalanches identified in the stress-strain curve in Fig. 5 (g) also indicate the loss of the plastic strain during the test.

3.3. Strain rate sensitivity of the gradient NC stainless steel

We perform strain rate jump nanoindentation for the NG, UFG, and CG 316L stainless steel at the depth of 2 μm, 300 μm, and 1500 μm from the topmost surface. Fig. 7 (a) shows the load-displacement curves. The maximum load of the NG, UFG and CG 316L stainless steel at a given strain rate are quite different. The load on the NG 316L stainless steel is much higher than that on the UFG and CG316L samples, which is consistent with the nanohardness measurement shown in Fig. 4. Another point worth noting is that there is stress pop-ins after the changes of the prescribed strain rate during the test. Fig. 7 (b) presents the corresponding nanohardness of the NG, UFG, and CG 316L stainless steel measured from the strain-rate jump nanoindentation tests. There is a significant increase of the load and nanohardness when the strain rate changes from 0.001 to 0.1s^{-1} for the NG and UFG 316L stainless steel. The nanohardness data is summarized in Table 1 and will be used to analyze the SRS of the 316L stainless steel of the grain size varying from nanometers to

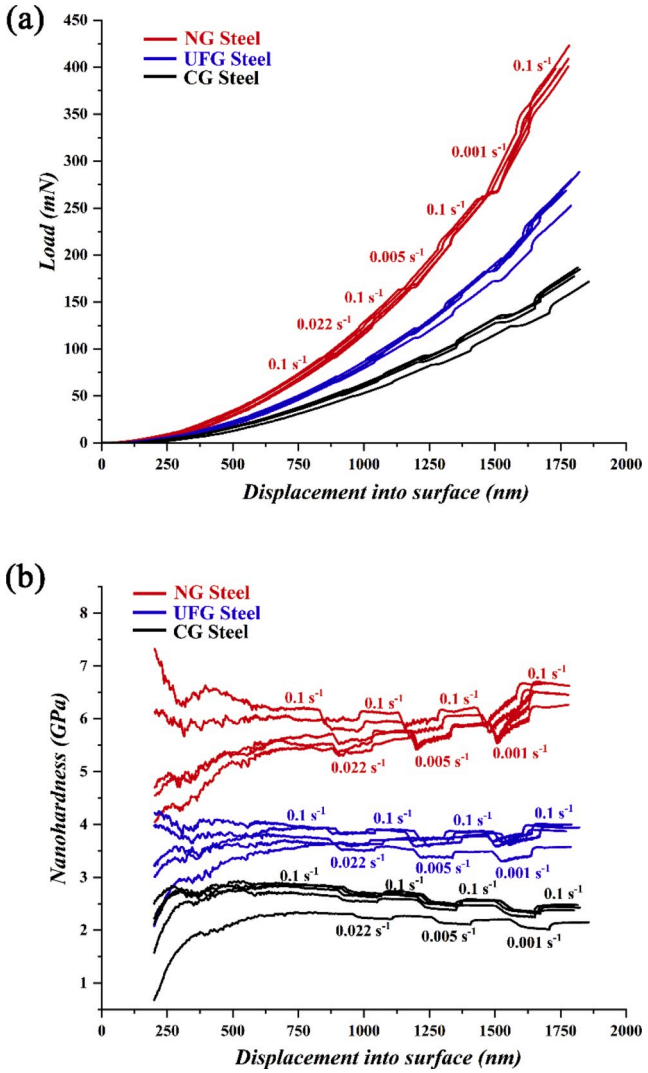

Fig. 7. (a) The load-displacement curves of the CG, UFG, and NG 316L stainless steel using the CSM mode of nanoindentation. The strain rates are set as 0.1 s^{-1}, 0.022 s^{-1}, 0.005 s^{-1}, and 0.001 s^{-1}. (b) The corresponding nanohardness of the CG, UFG and NG 316L stainless steel at different strain rates.

Table 1
Nanohardness of 316L stainless steel with the average grain size of 10 nm, 236 nm, and 28,000 nm measured at the strain rates of 0.1 s^{-1}, 0.022 s^{-1}, 0.005 s^{-1}, and 0.001 s^{-1}.

Average Grain size (nm)	Strain rate (s^{-1})	Nanohardness (GPa)					
		Test 1	Test 2	Test 3	Test 4	Test 5	Mean ± SD
10	0.1	6.647	6.741	6.735	6.622	6.468	6.64 ± 0.11
	0.022	6.412	6.448	6.575	6.310	6.252	6.40 ± 0.13
	0.005	6.332	6.504	6.291	6.139	6.024	6.26 ± 0.18
	0.001	5.890	6.270	6.357	6.160	6.300	6.20 ± 0.19
236	0.1	4.819	4.805	4.726	4.706	4.876	4.79 ± 0.07
	0.022	4.356	4.263	4.226	4.178	4.265	4.26 ± 0.06
	0.005	4.122	3.995	4.080	3.997	3.924	4.02 ± 0.08
	0.001	4.112	3.912	4.076	3.909	3.823	3.97 ± 0.12
28,000	0.1	3.844	3.727	3.966	3.699	3.836	3.81 ± 0.11
	0.022	3.237	3.097	3.403	3.064	3.246	3.21 ± 0.14
	0.005	2.912	2.780	3.024	2.713	2.907	2.87 ± 0.12
	0.001	2.679	2.585	2.792	2.483	2.674	2.64 ± 0.12

micrometers.

Fig. 8 plots the SRS of the NG, UFG, and CG 316L stainless steel using the nanohardness data in Table 1. The average m-value of the stainless steel with the average grain size of 10 nm, 236 nm, and 28 μm is 0.0103, 0.0392, and 0.0836, respectively. It should be noted that the average grain size of the UFG 316L stainless steel is calculated using the H–P equation (Yin et al., 2018a) with the nanohardness of 3.6 GPa instead of being determined by direct TEM characterization. Fig. 8 shows that the m-value of the NC 316L stainless steel is significantly smaller comparing to its coarse-grained counterparts. It is expected that the volume fractions of the grain boundaries, triple junctions, and intercrystallite defects significantly increase when the grain size of the metals and alloys are refined into the nanoscale. Therefore, the grain boundary-mediated activities, i.e. grain boundary sliding and coble creep, would become more active and lead to a higher rate sensitivity (Huang et al., 2010). By contrast, we find a significantly decreased SRS in the NC 316L stainless steel at the nanoscale. Wei et al. reported an in-depth study on the effect of NC and ultrafine grain sizes on the SRS of metals and alloys. They pointed out that while the SRS of the UFG/NC FCC metals increased, the SRS of UFG/NC BCC metals was much reduced compared to their coarse-grained counterparts (Wei et al., 2004a). We believe that the significantly reduced m-value of the NC 316L stainless steel is due to the phase transformation from the FCC austenite to the BCC martensite crystalline structure as identified by the XRD measurements in Fig. 3. The increase of the SRS has been observed in pure FCC metals copper (Chen et al., 2006; Cheng et al., 2005; Dao et al., 2006), Ni (Wang et al., 1997), and Au (Tanimoto et al., 1999), while the reduction of the SRS was reported in BCC metals Fe (Jang and Atzmon, 2003; Jia et al., 2003; Malow et al., 1998), Ta (Wei et al., 2003), and V (Wei et al., 2004b).

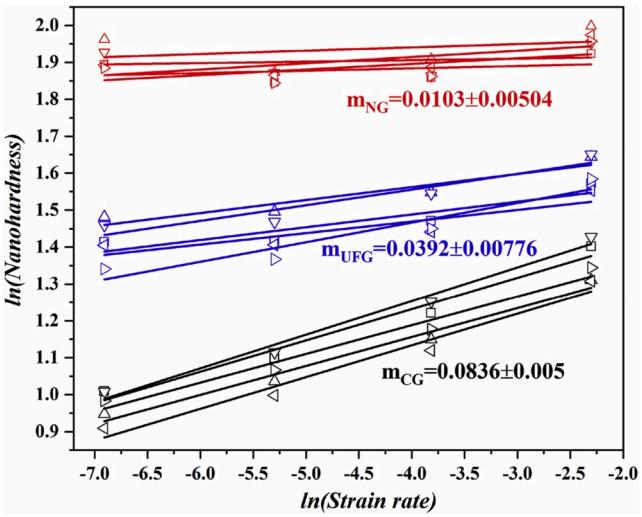

Fig. 8. The strain rate sensitivity of the NG, UFG, and CG 316L stainless steel measured by the strain rate jump nanoindentation test.

4. Discussion

4.1. Extremely fined nanocrystalline steel

One of the highlights of this study is that we successfully fabricate the extremely fined NC steel with the average grain size of 5 nm and confirm it using TEM as shown in Fig. 2 (b). Even though the thickness of this extremely fined NC stainless steel layer is only around 2–3 μm, it shows the outstanding capability of the USET comparing to other SPD methods. It is generally considered that the grain boundary energy would significantly increase when the grain structure of the metals is refined into the nanoscale, which results in the instability of the NC metals and alloys (Zhou et al., 2018). Nanograined structure even tends to coarsen at room temperature (Chookajorn et al., 2012; Weertman, 2012). During the grain refinement process of metals and alloys, high strain-rate, severe plastic deformation, and elevated temperature are always involved. Hence, it is a significant challenge to produce extremely fined NC steel by

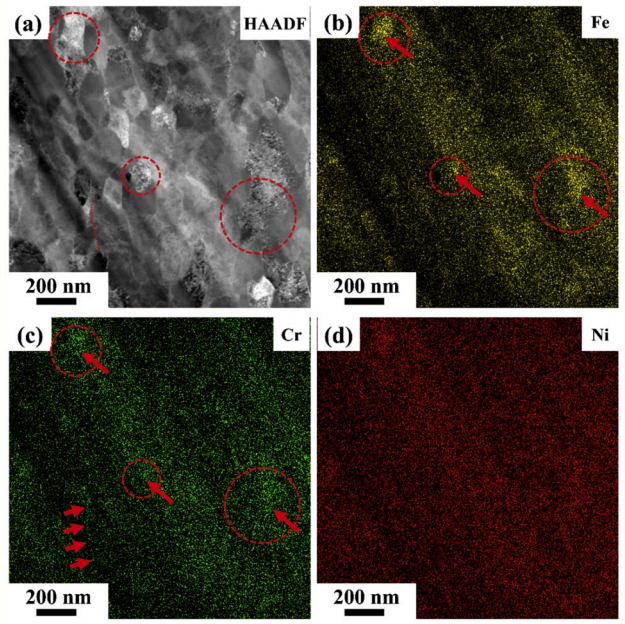

Fig. 9. Nanoscale precipitates embodied in the grains and along the grain boundaries suppresses the grain boundary and dislocation activities and contributes to the extraordinary mechanical strength of the NC steel. (a) HAADF-STEM image of the NC steel. (b)–(d) EDS mapping of Fe, Cr, and Ni at nanoscale in the NC steel.

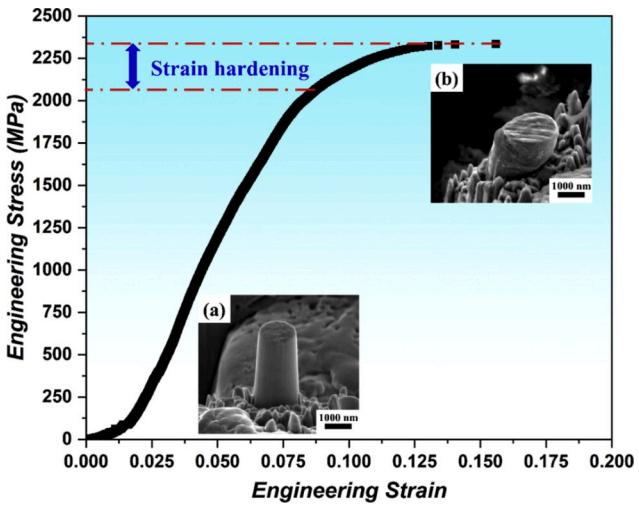

Fig. 10. Engineering stress-strain response of the extremely fined NC stainless steel with the grain size of 5–10 nm. The inset images (a) and (b) show the micropillar before the compression test and at the maximum strength of 2.3 GPa, respectively.

SPD methods at ambient temperature. During the USET, the target surface is impacted around 120 times per second per shot. In this work, 36 high-strength shots are placed on the ultrasonic surface within a diameter of 25.4 mm. This high-intense cyclical solid phase processing method allows the material undergo severe plastic deformation and element re-distribution simultaneously. This mechanism can enhance the grain stability by decreasing the grain boundary energy and reducing the pinning effect of element segregation/precipitation thermodynamically. The in-situ grain structure stability mechanism ensures the stability of the NC/UFG stainless steel during the grain refinement process and is the key to fabricate extremely fined NC stainless steel with the average grain size of 5 nm or less. Fig. 9 illustrates the STEM/EDS analysis of the NC stainless steel at the depth of 5–6 μm from the topmost surface. The average grain size is around 50 nm. Fig. 9 (a)–(d) shows the Z-contrast STEM/HAADF and the spatial distribution of Fe, Cr, and Ni in the NC 316L stainless steel at nanoscale. The HAADF signal in Fig. 9 (a) varies from grain to grain and some nanosized element segregation/precipitations embodied in the ultrafine grains can be clearly identified and circled by the red dashed lines. Red arrows are used to highlight the identified Fe/Cr-rich precipitations in Fig. 9 (a)–(c). In addition, Cr-rich segregation along the grain boundaries is identified and marked by the red dashed line in Fig. 9 (a) and represented by the red arrows in Fig. 9 (c). This confirms that the grain boundary energy can be largely reduced by the element segregation and precipitations at the nanoscale (Chookajorn et al., 2012; Kalidindi and Schuh, 2017), which results in the stable nanocrystalline structure that enables future grain refinement.

We want to point out that the micropillar at the depth of 5 μm in Fig. 5 is not the strongest sample in this work. The average grain size of the micropillar fabricated at the location of 5 μm is around 25–30 nm. The mechanical behavior of the extremely fined NC steel with the average grain size of 20 nm or less is measured by nanoindentation as shown in Fig. 4 (a). The maximum nanohardness of 6.1 GPa is found at the topmost surface of the treated sample. Hence, we expect that the yield strength of the extremely fined NC stainless steel can reach as high as 2.0 GPa. The thickness of the extremely fined NC 316L stainless steel is thin, only 2∼3 μm, as evident in Fig. 2 (a). Here we manage to fabricate a micropillar with the diameter of 1.5 μm and height of 3 μm at the topmost surface as shown in Fig. 10 (a). This micropillar is compressed using nanoindenter according to the experimental protocol describe in the Session 2.3. Fig. 10 plots the engineering strain-stress response of the micropillar. The yield strength and the ultimate strength are determined to be 2.1 GPa and 2.3 GPa, respectively. Fig. 10 (b) demonstrates the microstructure of the micropillar after the compression test. The micropillar deforms uniformly without slip bands at its outer surface. The strain hardening identified from the stress-strain curve implies that the grain boundaries in the micropillar accommodate dislocations of the NC steel when it undergoes plastic deformation.

4.2. Hall-Petch equation of the NC steel at nanoscale

The successful fabrication of such extremely fined NC steel provides us a research window to study the mechanical behavior of the NC steel with the grain size of 20 nm or less. In 2018, we reported the mechanical strength of the NC 316L stainless steel of the grain size of 25 nm. In this work, we push further the grain size down to ∼10 nm. Table 2 summarizes the experimental data of the NC 316L stainless steel resulted from our studies and other published papers. The Hall-Petch (H–P) relationship in equation (2) is often used to describe the dependence of the yield strength on the grain size of metals and alloys,

$$\sigma_y = \sigma_0 + K_y d^{1/2}, \tag{2}$$

Table 2
Yield strength and/or nanohardness of 316L stainless steel at nanoscale reported in literature and the results of this work.

Processing method	Phase condition	Average grain size (nm)	UTS (MPa)	Yield strength (MPa)	Elongation (%)	Hardness (HV10/GPa)	Ref.
USET	α + γ	10	2300	2100	–	–	This work
USET	α + γ	15	–	–	–	6.019 ± 0.15	This work
USET	α + γ	29	–	1906	–	5.875 ± 0.1	This work
USET	α + γ	42	–	–	–	5.77 ± 0.13	This work
USET	α + γ	58	–	–		5.57 ± 0.03	This work
USET	α + γ	115	–	–	–	5.44 ± 0.1	This work
USET	α + γ	168	–	1716	–	5.356 ± 0.1	This work
HPT at RT	100% γ	62	1790 ± 50	1360 ± 50	22.9 ± 0.2	4.9 ± 0.1	Wang et al. (2012)
HPT at 673K	α + γ	90		1720			Abramova et al. (2014)
ECAP at 423K with 4 passes	–	30-40 (inter-twin spacing)	1560 ± 40	1480 ± 40	0.5–1.6	–	Ueno et al. (2011)
7% CR at 523K + 95% CR at 258K + 1023 K/300s	95% γ	100	1304	–	–	–	Eskandari et al. (2009)
30% CR at 523 K + 95%CR at 258K + 1023 K/300s	95% γ	35 ± 5	1385	–	5.5	4950 HV	Eskandari et al. (2009)
80% CR at 77K + 873 k/600s	60% γ	100	1610	1280	3.2	5.4	Üçok et al. (1991)
SMAT	γ	40	1550 ± 80	1450 ± 60	3.4	4.5	Chen et al. (2005)

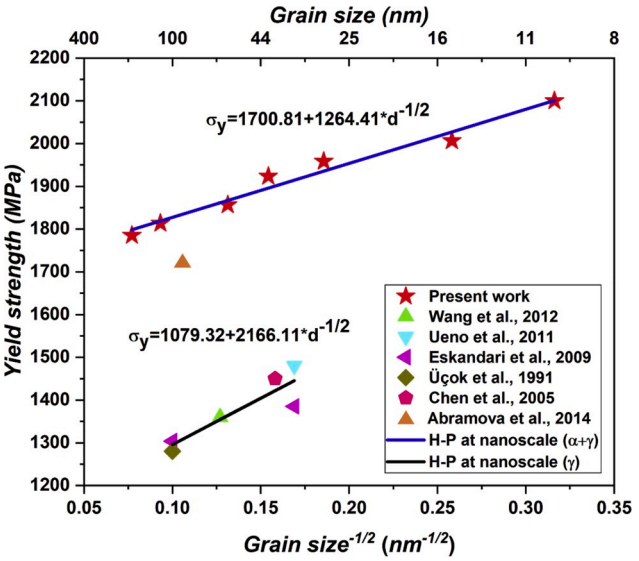

Fig. 11. The Hall-Petch plot of the NC 316L stainless steel of different phases at nanoscale.

where σ_y is the yield strength, d the average grain size, σ_0 the friction stress, and K_y a yield constant.

Ultrasonic assisted high-intense Strain Engineering Technology (USET); Cold rolling (CR); Mechanical Milling (MM); High Pressure Torsion (HPT); Ultimate Tensile Strength (UTS); Surface Mechanical Attrition Treatment (SMAT); Vacuum Hot Pressing (VHP); Room Temperature (RT).

Using the data presented in this work and those extrapolated from published literature in Table 2, we determine the H–P equation for the NC steel with the average grain size in the range of 10 nm–200 nm as follows:

$$\sigma_y = \begin{pmatrix} 1700.81 \\ 1079.32 \end{pmatrix} + \begin{pmatrix} 1264.41 \\ 2166.11 \end{pmatrix} * d^{-1/2} \qquad \begin{matrix} \alpha+\gamma \\ \gamma \end{matrix} . \tag{3}$$

Fig. 11 shows the H–P relationship of the NC 316L stainless steel at nanoscale with different phase conditions. The phase condition of the NC steel significantly affects its mechanical behavior. The NC steel with an α phase dominant structure has a higher friction stress than those with a γ phase dominant structure. This conclusion is achieved based on the analysis of the data obtained from this study and other published results. The formation of the martensite α phase and element segregation may influence the local short-range dislocation dynamics of kink pair formation at nanoscale. In-situ TEM mechanical tests should be conducted to give further detailed mechanistic understanding.

The yield strength of the NC 316L stainless steel with the grain size from 15 nm to 168 nm is estimated from the nanohardness test results. It is calculated using the following equation:

$$\sigma_y = H/3, \tag{4}$$

where σ_y is the yield strength and H is the nanohardness of the material.

One point worth noting is that the yield strength of the NC 316L stainless steel with the average grain size of 29 nm measured from the micropillar compression test is 1906 MPa, while the calculated yield strength from the nanohardness measurement is 1958 MPa. This deviation is mostly due to the contact angle between the surface of the flat tip and the top surface of the micropillar (Fei et al., 2012). The in-situ micropillar compression test has a better alignment for the measurement (Zhang et al., 2006). In this study, the yield strength calculated from equation (4) is utilized to determine the H–P relationship as shown in Fig. 11.

Moreover, it is conceived that the H–P relationship may not hold in NC metals when the grain size is refined down to nanometer scale. However, according to our nanohardness and micropillar compression test results, the H–P relationship remains correct when the grain size is reduced to several nanometers for the NC 316L stainless steel fabricated by the USET. In 2017, Hu et al. reported that, with grain boundary stabilization and alloying element segregation, ultrahigh hardness was achieved in the extremely fined NC nickel-molybdenum alloys with the average grain size of 10 nm or less (Hu et al., 2017). As demonstrated in Fig. 9, the alloying elements segregation and second phases are characterized in the as-fabricated NC 316L stainless steel. The element segregation and secondary phases can stabilize the grain structure while the H–P equation can still correctly describe the mechanical behavior the NC stainless steel with the grain size of several nanometers. Another example is that Chen et al. produced a NC 316L stainless steel with the average grain size of 40 nm using the surface mechanical attrition treatment (SMAT). This material also follows the H–P relationship extrapolated from the CG materials (Chen et al., 2005). Hence, the USET and SMAT, which introduce high-intense plastic deformation and physical metallurgy into the target materials, can be used as an effective method to fabricate ultrastrong metal and alloys with extremely fined grain structure.

4.3. Rate-dependent modeling at nanoscale

We adopt and validate a rate dependent constitutive model for BCC metals and alloys developed by Jia et al. (2003) using the experimental results. The constitutive model for the gradient NC stainless steel will be valuable for future numerical analysis of the material of various boundary conditions. It is well known that dislocations are the major carriers of plastic deformation in metals and alloys of the grain size larger than 30 nm. In BCC crystals, screw dislocation cores are dissociated into non-planar configurations and the mobility of the edge component of the dislocation loops is much higher than that of the screw component (Duesbery and Vitek, 1998). The primary barrier to the motion of screw dislocations is the lattice-related Peierls barriers. The screw dislocations move by the nucleation and propagation of kink pairs and the screw mobility is primarily controlled by the kink nucleation at low temperatures. The kink pair nucleation rate v_k is calculated in the following equation,

$$v_k = v_{k0}\exp\left(-\frac{\Delta G_k}{k_B T}\right), \tag{5}$$

where v_{k0} is the attempt frequency and ΔG_k is the activation energy for the kink-pair nucleation. The dislocation velocity v_d is then determined by

$$v_d = \lambda v_k = \lambda v_{k0}\exp\left(-\frac{\Delta G_k}{k_B T}\right), \tag{6}$$

where λ is the distance between the Peierls barriers, which is of the same order of magnitude of the Burgers vector in BCC metals. The rate of plastic deformation $\dot{\varepsilon}$ follows

$$\dot{\varepsilon} = \rho_m b v_d = \rho_m b \lambda v_{k0}\exp\left(-\frac{\Delta G_k}{k_B T}\right), \tag{7}$$

where ρ_m is the mobile dislocation density and b is the Burgers vector. The dependence of the activation energy on the stress can be defined using the function proposed by Kocks, Argon & Ashby (KAA) (MF, 1975) as noted in the following equation,

$$\Delta G_k = \Delta G_{k0}\left\{1-\left(\frac{\widehat{\sigma}}{\overline{\sigma}_0}\right)^p\right\}^q, \tag{8}$$

where $\widehat{\sigma}$ is the effective stress for the thermally activated process and $\overline{\sigma}_0$ is a material parameter determined by the microstructure of the material, e.g. the grain size d. p and q are the parameters that define the barrier shape. The commonly used values for BCC metals are $p = 1/2$ and $q = 3/2$ according to the previous literature (Jia et al., 2003). Combining equations (5) and (6), the effective thermally assisted "Peierls stress" $\widehat{\sigma}$ can be formulated as follows

$$\widehat{\sigma} = \overline{\sigma}_0\left[1-\left\{\frac{k_B T}{\Delta G_{k0}} ln\left(\frac{\rho_m b \lambda v_{k0}}{\dot{\varepsilon}}\right)\right\}^{\frac{1}{q}}\right]^{\frac{1}{p}}. \tag{9}$$

It should be noted that the effective thermally assisted Peierls stress $\widehat{\sigma}$ is the component of the flow stress σ related to the thermally active motions over the short-range barriers. The "athermal" stress that needed to overcome the long-range barriers of the moving dislocations should be added in the constitutive function of the material, equation (10). The athermal stress $\sigma_{athermal}$, is arising from the grain boundaries and is denoted in the Hall-Petch form in equation (11). According to the strain-stress curves obtained from the micropillar compression tests in Fig. 5, strain hardening of the NC stainless steel at nanoscale can be clearly identified. Hence, the strain hardening function $g(\varepsilon)$ should be included in equation (12) to formulate the constitutive equation.

$$\sigma = \sigma_{athermal} + \overline{\sigma}_0\left[1-\left\{\frac{k_B T}{\Delta G_{k0}} ln\left(\frac{\rho_m b \lambda v_{k0}}{\dot{\varepsilon}}\right)\right\}^{\frac{1}{q}}\right]^{\frac{1}{p}} \tag{10}$$

$$\sigma_{athermal} = \sigma_0 + K_y d^{-1/2} + g(\varepsilon) \tag{11}$$

$$\sigma = \sigma_0 + K_y d^{-1/2} + g(\varepsilon) + \overline{\sigma}_0\left[1-\left\{\frac{k_B T}{\Delta G_{k0}} ln\left(\frac{\rho_m b \lambda v_{k0}}{\dot{\varepsilon}}\right)\right\}^{\frac{1}{q}}\right]^{\frac{1}{p}} \tag{12}$$

The term $g(\varepsilon)$ in equation (12) represents the strain hardening of the NC metal during plastic deformation. The experimental data in this work unfortunately cannot fully capture the effect of the strain rate on the strain hardening of the NG/UFG 316L stainless steel. A more careful design of micropillar compression tests of the gradient nanocrystalline 316L stainless steel subject to different strain rates should be performed to determine the flow stress (σ) upon strain hardening in future studies. Here we have simplified the functional dependence of the yield strength (σ_y) on the grain size (d) and the strain rate ($\dot{\varepsilon}$) of the deformed micropillar as follows without

considering the strain hardening term

$$\sigma_y = f(\mathrm{d}, \dot{\varepsilon}) = \sigma_0 + K_y d^{-1/2} + \overline{\sigma}_0 \left[1 - \left\{ \frac{k_B T}{\Delta G_{k0}} ln\left(\frac{\rho_m b \lambda \nu_{k0}}{\dot{\varepsilon}} \right) \right\}^{\frac{1}{q}} \right]^{\frac{1}{p}}. \tag{13}$$

We adopt the following parameters: $p = 1$ and $q = 3/2$ for BCC metals, $\rho_m \sim 10^{15} m^{-2}$, Burgers vector $b = 3 \times 10^{-10}\ m$, $\lambda = 1 \times 10^{-10}\ m$, the attempt frequency $\nu_{k0} = \sim 10^{12} s^{-1}$, $\Delta G_{k0} = 0.675$ eV for BCC metals, and the operating temperature 300 K. With $A = \frac{k_B T}{\Delta G_{k0}}$ and $\mathrm{B} = \rho_m b \lambda \nu_{k0}$, it yields

$$\sigma_y = f(\mathrm{d}, \dot{\varepsilon}) = \sigma_0 + K_y d^{-1/2} + \overline{\sigma}_0 \left[1 - \left\{ A \times ln\left(\frac{\mathrm{B}}{\dot{\varepsilon}} \right) \right\}^{\frac{2}{3}} \right], \tag{14}$$

where $A = 3.83 \times 10^{-2}$ and $B = 1 \times 10^7$ in the above equation. The physical mechanism underlying each term in equation (14) should be understood. The first term $\sigma_0 + K_y d^{-1/2}$ denotes the long-range grain boundary strengthening of the NC steel. It is unrelated with the strain rate. Hereby, the BCC α phase dominant H–P equation written in equation (3) will be used in equation (14). Based on the experimental data at the strain rate of 0.05 s^{-1} and the SRS value of 0.0103, the H–P equation of the tested data at the strain rate of 1×10^{-5} s^{-1} can be derived and will be used. The second term $\overline{\sigma}_0 \left[1 - \left\{ A \times ln\left(\frac{\mathrm{B}}{\dot{\varepsilon}} \right) \right\}^{\frac{2}{3}} \right]$ is the SRS portion of the NC steel. Given $\overline{\sigma}_0 =$ 1400 *MPa* and combining with the H–P equation, we can obtain the complete rate-dependent constitutive law of the NC steel at nanoscale. Fig. 12 shows the validation of the developed rate-dependent constitutive equation. The model is in excellent agreement with the experimental data. The error analysis shows that the deviation between the theoretical values and the experimental results for the NC steel of the grain size of 15 nm, 29 nm, 42 nm, 58 nm, 115 nm, and 168 nm is 1.27%, −0.46%, −0.53%, 1.53%,1.52%, and 2.05%, respectively. The error e is calculated using the following equation:

$$e = \left(\frac{\sigma_{cal} - \sigma_{exp}}{\sigma_{exp}} \right) \times 100\%, \tag{15}$$

where σ_{cal} is the calculated yield strength and σ_{exp} is the experimental value.

It should be noted that the rate-dependent constitutive equation is validated for the NC steel of the grain size of 10 nm–200 nm. For the CG steel of larger grains and FCC metals, this constitutive equation may not be suitable. According to the TEM diffraction patterns in Fig. 2 (e)–(g), the fraction of the BCC α phases gradually decreases with the increase of the grain size or the depth from the topmost surface. The coexistence of the BCC α phases and the FCC γ phases can result in difference between the modeling results and the experimental values. Fig. 12 (a) shows that the deviation between the theoretical prediction and the experimental data indeed enlarges as the grain size increases. While the constitutive model is meritorious in describing the mechanical behavior of the NC 316L stainless steel at nanoscale, the limitation of this model should be acknowledged in future studies.

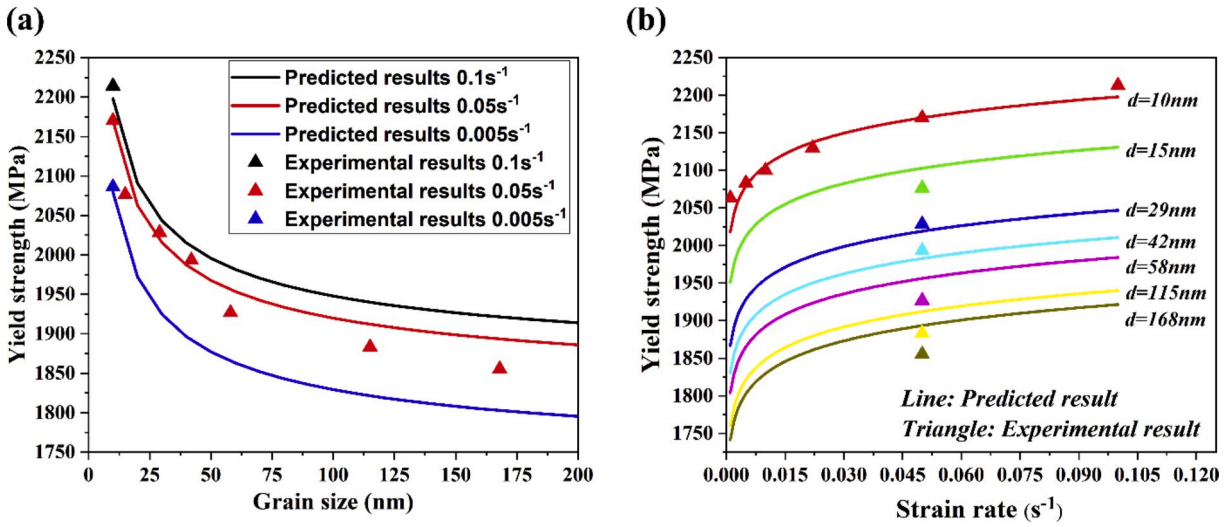

Fig. 12. Validation of the rate-dependent constitutive model of the gradient NC steel. (a) Yield strength versus the average grain size of the NC steel deformed at different strain rates. (b) Yield strength against the strain rate of the NC steel of various grain sizes at nanoscale.

5. Conclusions

We report a successful fabrication of gradient NC 316L stainless steel using an ultrasonic strain engineering technology at ambient temperature. The material is fully characterized using advanced tools at nanoscale to determine its unprecedented mechanical performance. Major conclusions are as follows:

(a) The NC steel has a gradient layer thickness of over 500 μm. The mechanical property is elastically homogenous but plastically gradient in nature;
(b) We fabricate an extremely fined NC steel of the grain size of 5 nm. The in-situ grain boundary stability mechanism is the key to achieve such extremely fined NC structure via severe plastic deformation at ambient temperature;
(c) We determine the relationship between the SRS and the grain size of the NC steel. The SRS decreases when the grain size of the NC steel reduces. This behavior is attributed to the phase transformation of the NC 316L stainless steel from FCC austenite to BCC martensite structures as well as the nanosized intermetallic precipitates along the grain boundaries;
(d) The gradient NC steel exhibits a yield strength of 2.1 GPa which is almost 10 times higher than its CG counterparts. The Hall-Petch strengthening relationship remains hold for the NC steel;
(e) We adopt and validate a rate-dependent constitutive model for the NC steel at nanoscale that can be widely used in future studies to simulate the mechanical response of the NC materials deformed at different strain rates and under various boundary conditions.

Funding

This research did not receive any specific grant from funding agencies in the public, commercial, or not-for-profit sectors.

Declaration of competing interest

The authors declare that they have no known competing financial interests or personal relationships that could have appeared to influence the work reported in this paper.

CRediT authorship contribution statement

Fei Yin: Conceptualization, Methodology, Writing - original draft. **Shan Hu:** Data curation, Writing - original draft. **Rong Xu:** Investigation. **Xinghui Han:** Validation. **Dongsheng Qian:** Validation. **Wenting Wei:** Validation. **Lin Hua:** Supervision, Writing - review & editing. **Kejie Zhao:** Supervision, Writing - review & editing.

Acknowledgements

The authors would like to thank the supports from the Purdue Center for Materials Processing Research, Center for Technology Development at Purdue University, School of Mechanical Engineering at Purdue University, Hubei Key Laboratory of Advanced Technology for Automotive Components and Hubei Collaborative Innovation Center for Automotive Components Technology at Wuhan University of Technology.

Appendix A. Supplementary data

Supplementary data to this article can be found online at https://doi.org/10.1016/j.ijplas.2020.102696.

References

Abramova, M., Enikeev, N., Valiev, R., Etienne, A., Radiguet, B., Ivanisenko, Y., Sauvage, X., 2014. Grain boundary segregation induced strengthening of an ultrafine-grained austenitic stainless steel. Mater. Lett. 136, 349–352. https://doi.org/10.1016/j.matlet.2014.07.188.

Chen, J., Lu, L., Lu, K., 2006. Hardness and strain rate sensitivity of nanocrystalline Cu. Scripta Mater. 54, 1913–1918. https://doi.org/10.1016/j.scriptamat.2006.02.022.

Chen, X., Lu, J., Lu, L., Lu, K., 2005. Tensile properties of a nanocrystalline 316L austenitic stainless steel. Scripta Mater. 52, 1039–1044. https://doi.org/10.1016/j.scriptamat.2005.01.023.

Cheng, S., Ma, E., Wang, Y., Kecskes, L., Youssef, K., Koch, C., Trociewitz, U., Han, K., 2005. Tensile properties of in situ consolidated nanocrystalline Cu. Acta Mater. 53, 1521–1533. https://doi.org/10.1016/j.actamat.2004.12.005.

Chinh, N.Q., Győri, T., Valiev, R.Z., Szommer, P., Varga, G., Havancsák, K., Langdon, T.G., 2012. Observations of unique plastic behavior in micro-pillars of an ultrafine-grained alloy. MRS Commun. 2, 75–78. https://doi.org/10.1557/mrc.2012.11.

Chookajorn, T., Murdoch, H.A., Schuh, C.A., 2012. Design of stable nanocrystalline alloys. Science 337, 951–954. https://doi.org/10.1126/science.1224737.

Dao, M., Lu, L., Asaro, R., De Hosson, J.T.M., Ma, E., 2007. Toward a quantitative understanding of mechanical behavior of nanocrystalline metals. Acta Mater. 55, 4041–4065. https://doi.org/10.1016/j.actamat.2007.01.038.

Dao, M., Lu, L., Shen, Y., Suresh, S., 2006. Strength, strain-rate sensitivity and ductility of copper with nanoscale twins. Acta Mater. 54, 5421–5432. https://doi.org/10.1016/j.actamat.2006.06.062.

Duesbery, M.a.-S., Vitek, V., 1998. Plastic anisotropy in bcc transition metals. Acta Mater. 46, 1481–1492. https://doi.org/10.1016/S1359-6454(97)00367-4.
Eskandari, M., Najafizadeh, A., Kermanpur, A., 2009. Effect of strain-induced martensite on the formation of nanocrystalline 316L stainless steel after cold rolling and annealing. Mater. Sci. Eng., A 519, 46–50. https://doi.org/10.1016/j.msea.2009.04.038.
Fang, T., Li, W., Tao, N., Lu, K., 2011. Revealing extraordinary intrinsic tensile plasticity in gradient nano-grained copper. Science 331, 1587–1590. https://doi.org/10.1126/science.1200177.
Farrokh, B., Khan, A.S., 2009. Grain size, strain rate, and temperature dependence of flow stress in ultra-fine grained and nanocrystalline Cu and Al: synthesis, experiment, and constitutive modeling. Int. J. Plast. 25, 715–732. https://doi.org/10.1016/j.ijplas.2008.08.001.
Fei, H., Abraham, A., Chawla, N., Jiang, H., 2012. Evaluation of micro-pillar compression tests for accurate determination of elastic-plastic constitutive relations. J. Appl. Mech. 79, 061011 https://doi.org/10.1115/1.4006767.
Hu, J., Shi, Y., Sauvage, X., Sha, G., Lu, K., 2017. Grain boundary stability governs hardening and softening in extremely fine nanograined metals. Science 355, 1292–1296. https://doi.org/10.1126/science.aal5166.
Huang, P., Wang, F., Xu, M., Xu, K., Lu, T., 2010. Dependence of strain rate sensitivity upon deformed microstructures in nanocrystalline Cu. Acta Mater. 58, 5196–5205. https://doi.org/10.1016/j.actamat.2010.05.055.
Jang, D., Atzmon, M., 2003. Grain-size dependence of plastic deformation in nanocrystalline Fe. J. Appl. Phys. 93, 9282–9286. https://doi.org/10.1063/1.1569035.
Jia, D., Ramesh, K., Ma, E., 2003. Effects of nanocrystalline and ultrafine grain sizes on constitutive behavior and shear bands in iron. Acta Mater. 51, 3495–3509. https://doi.org/10.1016/S1359-6454(03)00169-1.
Kabirian, F., Khan, A.S., Pandey, A., 2014. Negative to positive strain rate sensitivity in 5xxx series aluminum alloys: experiment and constitutive modeling. Int. J. Plast. 55, 232–246. https://doi.org/10.1016/j.ijplas.2013.11.001.
Kalidindi, A.R., Schuh, C.A., 2017. Stability criteria for nanocrystalline alloys. Acta Mater. 132, 128–137. https://doi.org/10.1016/j.actamat.2017.03.029.
Khan, A.S., Farrokh, B., Takacs, L., 2008. Effect of grain refinement on mechanical properties of ball-milled bulk aluminum. Mater. Sci. Eng., A 489, 77–84. https://doi.org/10.1016/j.msea.2008.01.045.
Khan, A.S., Liu, H., 2012. Variable strain rate sensitivity in an aluminum alloy: response and constitutive modeling. Int. J. Plast. 36, 1–14. https://doi.org/10.1016/j.ijplas.2012.02.001.
Khan, A.S., Meredith, C.S., 2010. Thermo-mechanical response of Al 6061 with and without equal channel angular pressing (ECAP). Int. J. Plast. 26, 189–203. https://doi.org/10.1016/j.ijplas.2009.07.002.
Khan, A.S., Suh, Y.S., Chen, X., Takacs, L., Zhang, H., 2006. Nanocrystalline aluminum and iron: mechanical behavior at quasi-static and high strain rates, and constitutive modeling. Int. J. Plast. 22, 195–209. https://doi.org/10.1016/j.ijplas.2004.07.008.
Khodabakhshi, F., Farshidianfar, M., Gerlich, A., Nosko, M., Trembošová, V., Khajepour, A., 2019. Microstructure, strain-rate sensitivity, work hardening, and fracture behavior of laser additive manufactured austenitic and martensitic stainless steel structures. Mater. Sci. Eng., A 756, 545–561. https://doi.org/10.1016/j.msea.2019.04.065.
Lei, Y., Wang, Z., Xu, J., Lu, K., 2019. Simultaneous enhancement of stress-and strain-controlled fatigue properties in 316L stainless steel with gradient nanostructure. Acta Mater. 168, 133–142. https://doi.org/10.1016/j.actamat.2019.02.008.
Li, J., Soh, A., 2012. Modeling of the plastic deformation of nanostructured materials with grain size gradient. Int. J. Plast. 39, 88–102. https://doi.org/10.1016/j.ijplas.2012.06.004.
Li, Z., Voisin, T., McKeown, J.T., Ye, J., Braun, T., Kamath, C., King, W.E., Wang, Y.M., 2019. Tensile properties, strain rate sensitivity, and activation volume of additively manufactured 316L stainless steels. Int. J. Plast. 120, 395–410. https://doi.org/10.1016/j.ijplas.2019.05.009.
Liu, J., Khan, A.S., Takacs, L., Meredith, C.S., 2015. Mechanical behavior of ultrafine-grained/nanocrystalline titanium synthesized by mechanical milling plus consolidation: experiments, modeling and simulation. Int. J. Plast. 64, 151–163. https://doi.org/10.1016/j.ijplas.2014.08.007.
Lu, X., Zhang, X., Shi, M., Roters, F., Kang, G., Raabe, D., 2019. Dislocation mechanism based size-dependent crystal plasticity modeling and simulation of gradient nano-grained copper. Int. J. Plast. 113, 52–73. https://doi.org/10.1016/j.ijplas.2018.09.007.
Maier-Kiener, V., Durst, K., 2017. Advanced nanoindentation testing for studying strain-rate sensitivity and activation volume. JOM 69, 2246–2255. https://doi.org/10.1007/s11837-017-2536-y.
Maier, V., Durst, K., Mueller, J., Backes, B., Höppel, H.W., Göken, M., 2011. Nanoindentation strain-rate jump tests for determining the local strain-rate sensitivity in nanocrystalline Ni and ultrafine-grained Al. J. Mater. Res. 26, 1421–1430. https://doi.org/10.1557/jmr.2011.156.
Malow, T., Koch, C., Miraglia, P., Murty, K., 1998. Compressive mechanical behavior of nanocrystalline Fe investigated with an automated ball indentation technique. Mater. Sci. Eng., A 252, 36–43. https://doi.org/10.1016/S0921-5093(98)00661-3.
McDowell, D.L., 2010. A perspective on trends in multiscale plasticity. Int. J. Plast. 26, 1280–1309. https://doi.org/10.1016/j.ijplas.2010.02.008.
Meredith, C.S., Khan, A.S., 2012. Texture evolution and anisotropy in the thermo-mechanical response of UFG Ti processed via equal channel angular pressing. Int. J. Plast. 30, 202–217. https://doi.org/10.1016/j.ijplas.2011.10.006.
MF, A., 1975. Thermodynamics and kinetics of slip. Prog. Mater. Sci. 19, 1–281. https://doi.org/10.1016/0079-6425(75)90005-5.
Miyamoto, H., Ota, K., Mimaki, T., 2006. Viscous nature of deformation of ultra-fine grain aluminum processed by equal-channel angular pressing. Scripta Mater. 54, 1721–1725. https://doi.org/10.1016/j.scriptamat.2006.02.016.
Mohebbi, M.S., Akbarzadeh, A., 2017. Development of equations for strain rate sensitivity of UFG aluminum as a function of strain rate. Int. J. Plast. 90, 167–176. https://doi.org/10.1016/j.ijplas.2017.01.003.
Ovid'Ko, I., Sheinerman, A., 2017. Grain boundary sliding, triple junction disclinations and strain hardening in ultrafine-grained and nanocrystalline metals. Int. J. Plast. 96, 227–241. https://doi.org/10.1016/j.ijplas.2017.05.005.
Ovid'Ko, I., Valiev, R., Zhu, Y., 2018. Review on superior strength and enhanced ductility of metallic nanomaterials. Prog. Mater. Sci. 94, 462–540. https://doi.org/10.1016/j.pmatsci.2018.02.002.
Padilla, H., Boyce, B., 2010. A review of fatigue behavior in nanocrystalline metals. Exp. Mech. 50, 5–23. https://doi.org/10.1007/s11340-009-9301-2.
Rakita, M., Wang, M., Han, Q., Liu, Y., Yin, F., 2013. Ultrasonic shot peening. Int. J. Comput. Mater. Sci. Surf. Eng. 5, 189–209. https://doi.org/10.1504/IJCMSSE.2013.056948.
Schwaiger, R., Moser, B., Dao, M., Chollacoop, N., Suresh, S., 2003. Some critical experiments on the strain-rate sensitivity of nanocrystalline nickel. Acta Mater. 51, 5159–5172. https://doi.org/10.1016/S1359-6454(03)00365-3.
Tanimoto, H., Sakai, S., Mizubayashi, H., 1999. Mechanical property of high density nanocrystalline gold prepared by gas deposition method. Nanostruct. Mater. 12, 751–756. https://doi.org/10.1016/S0965-9773(99)00230-5.
Üçok, İ., Ando, T., Grant, N.J., 1991. Property enhancement in Type 316L stainless steel by spray forming. Mater. Sci. Eng., A 133, 284–287. https://doi.org/10.1016/0921-5093(91)90070-4.
Ueno, H., Kakihata, K., Kaneko, Y., Hashimoto, S., Vinogradov, A., 2011. Enhanced fatigue properties of nanostructured austenitic SUS 316L stainless steel. Acta Mater. 59, 7060–7069. https://doi.org/10.1016/j.actamat.2011.07.061.
Wang, H., Shuro, I., Umemoto, M., Ho-Hung, K., Todaka, Y., 2012. Annealing behavior of nano-crystalline austenitic SUS316L produced by HPT. Mater. Sci. Eng., A 556, 906–910. https://doi.org/10.1016/j.msea.2012.07.089.
Wang, N., Wang, Z., Aust, K., Erb, U., 1997. Room temperature creep behavior of nanocrystalline nickel produced by an electrodeposition technique. Mater. Sci. Eng., A 237, 150–158. https://doi.org/10.1016/S0921-5093(97)00124-X.
Weertman, J.R., 2012. Retaining the nano in nanocrystalline alloys. Science 337, 921–922. https://doi.org/10.1126/science.1226724.
Wei, Q., Cheng, S., Ramesh, K., Ma, E., 2004a. Effect of nanocrystalline and ultrafine grain sizes on the strain rate sensitivity and activation volume: fcc versus bcc metals. Mater. Sci. Eng., A 381, 71–79. https://doi.org/10.1016/j.msea.2004.03.064.
Wei, Q., Jiao, T., Mathaudhu, S., Ma, E., Hartwig, K., Ramesh, K., 2003. Microstructure and mechanical properties of tantalum after equal channel angular extrusion (ECAE). Mater. Sci. Eng., A 358, 266–272. https://doi.org/10.1016/S0921-5093(03)00305-8.

Wei, Q., Jiao, T., Ramesh, K., Ma, E., 2004b. Nano-structured vanadium: processing and mechanical properties under quasi-static and dynamic compression. Scripta Mater. 50, 359–364. https://doi.org/10.1016/j.scriptamat.2003.10.010.

Xu, J., Li, J., Shi, L., Shan, D., Guo, B., 2015. Effects of temperature, strain rate and specimen size on the deformation behaviors at micro/meso-scale in ultrafine-grained pure Al. Mater. Char. 109, 181–188. https://doi.org/10.1016/j.matchar.2015.10.003.

Yin, F., Cheng, G.J., Xu, R., Zhao, K., Li, Q., Jian, J., Hu, S., Sun, S., An, L., Han, Q., 2018a. Ultrastrong nanocrystalline stainless steel and its Hall-Petch relationship in the nanoscale. Scripta Mater. 155, 26–31. https://doi.org/10.1016/j.scriptamat.2018.06.014.

Yin, F., Han, Q., Rakita, M., Wang, M., Hua, L., Wang, C., 2015a. Numerical modelling and experimental approach for shot velocity evaluation during ultrasonic shot peening. Int. J. Comput. Mater. Sci. Surf. Eng. 6, 97–110. https://doi.org/10.1504/IJCMSSE.2015.071646.

Yin, F., Hu, S., Hua, L., Wang, X., Suslov, S., Han, Q., 2015b. Surface nanocrystallization and numerical modeling of low carbon steel by means of ultrasonic shot peening. Metall. Mater. Trans. Phys. Metall. Mater. Sci. 46A, 1253–1261. https://doi.org/10.1007/s11661-014-2689-z.

Yin, F., Hua, L., Wang, X., Rakita, M., Han, Q., 2014. Numerical modelling and experimental approach for surface morphology evaluation during ultrasonic shot peening. Comput. Mater. Sci. 92, 28–35. https://doi.org/10.1016/j.commatsci.2014.05.011.

Yin, F., Liu, Y., Xu, R., Zhao, K., Partin, A., Han, Q., 2018b. Nanograined surface fabricated on the pure copper by ultrasonic shot peening and an energy-density based criterion for peening intensity quantification. J. Manuf. Process. 32, 656–663. https://doi.org/10.1016/j.jmapro.2018.04.003.

Yin, F., Rakita, M., Hu, S., Han, Q., 2017. Overview of ultrasonic shot peening. Surf. Eng. 1–16. https://doi.org/10.1080/02670844.2017.1278838.

Yin, F., Xu, R., Hu, S., Zhao, K., Yang, S., Kuang, S., Li, Q., Han, Q., 2018c. Enhanced mechanical and biological performance of an extremely fine nanograined 316L stainless steel cell–substrate interface fabricated by ultrasonic shot peening. ACS Biomater. Sci. Eng. 4, 1609–1621. https://doi.org/10.1016/j.matlet.2016.11.077.

Yin, F., Yang, S., Hu, S., Kuang, S., Han, Q., 2016. Enhanced human osteoblast cell functions by “net-like” nanostructured cell-substrate interface in orthopedic applications. Mater. Lett. 189, 275–278. https://doi.org/10.1016/j.matlet.2016.11.077.

Yuan, F., Yan, D., Sun, J., Zhou, L., Zhu, Y., Wu, X., 2019. Ductility by shear band delocalization in the nano-layer of gradient structure. Mater. Res. Lett. 7, 12–17. https://doi.org/10.1080/21663831.2018.1546238.

Zhang, H., Schuster, B.E., Wei, Q., Ramesh, K.T., 2006. The design of accurate micro-compression experiments. Scripta Mater. 54, 181–186. https://doi.org/10.1016/j.scriptamat.2005.06.043.

Zhang, J., Liu, G., Sun, J., 2013. Strain rate effects on the mechanical response in multi-and single-crystalline Cu micropillars: grain boundary effects. Int. J. Plast. 50, 1–17. https://doi.org/10.1016/j.ijplas.2013.03.009.

Zhang, Z., Jun, T.-S., Britton, T.B., Dunne, F.P., 2016. Intrinsic anisotropy of strain rate sensitivity in single crystal alpha titanium. Acta Mater. 118, 317–330. https://doi.org/10.1016/j.actamat.2016.07.044.

Zhao, L., Guo, Q., Li, Z., Li, Z., Fan, G., Xiong, D.-B., Su, Y., Zhang, J., Tan, Z., Zhang, D., 2018. Strain-rate dependent deformation mechanism of graphene-Al nanolaminated composites studied using micro-pillar compression. Int. J. Plast. 105, 128–140. https://doi.org/10.1016/j.ijplas.2018.02.006.

Zhou, J., Sun, Z., Kanouté, P., Retraint, D., 2017. Effect of surface mechanical attrition treatment on low cycle fatigue properties of an austenitic stainless steel. Int. J. Fatig. 103, 309–317. https://doi.org/10.1016/j.ijfatigue.2017.06.011.

Zhou, X., Li, X., Lu, K., 2018. Enhanced thermal stability of nanograined metals below a critical grain size. Science 360, 526–530. https://doi.org/10.1126/science.aar6941.